symmetry

MDPI

*Article*

# Evaluation of Shear Stress Transport, Large Eddy Simulation and Detached Eddy Simulation for the Flow around a Statically Loaded Tire

**Haichao Zhou [1,2,*], Huiyun Li [1], Qingyun Chen [1] and Lingxin Zhang [2]**

[1] School of Automotive and Traffic Engineering, Jiangsu University, Zhenjiang 212013, China; 2221904078@stmail.ujs.edu.cn (H.L.); 2221904063@stmail.ujs.edu.cn (Q.C.)
[2] AEOLUS Tyre Co., Ltd., Jiaozuo 454003, China; Zhanglingxin@rubber.chemchina.com
* Correspondence: hczhou@ujs.edu.cn; Tel.: +86-150-5292-9623

**Abstract:** To select a more suitable turbulence model to study tire aerodynamics, the characteristics of a deformed profile of a 185/65 R14 passenger tire were reproduced using 3D printing technology. Based on the distance from automobile chassis to the ground, a partially loaded tire model with a height of 150 mm was selected in this paper, and the surface pressure coefficient of the tire model was determined using a wind tunnel test. A computational fluid dynamics (CFD) model was established according to the tire wind tunnel test. The surface pressure coefficient results of three turbulence models, shear stress transport (SST) k-ω, large eddy simulation (LES), and detached eddy simulation (DES) were obtained. Compared with the wind tunnel test results, the mean relative errors of the surface pressure coefficients predicted using SST, LES, and DES in the longitudinal section were 22.4%, 20.9%, and 14.8%, respectively. The LES and DES can capture details of the unsteady flow field that were not predicted by SST. By synthetically analyzing the results of the surface pressure coefficient and flow fields, the DES model is more advantageous than the other two models in predicting the flow characteristics around a statically loaded tire. This study can help designers in the tire industry to apply these cost-effective tools for minimizing the aerodynamic drag of a new tire design.

**Keywords:** tire aerodynamics; turbulence model; wind tunnel test; flow field; numerical simulation



**Citation:** Zhou, H.; Li, H.; Chen, Q.; Zhang, L. Evaluation of Shear Stress Transport, Large Eddy Simulation and Detached Eddy Simulation for the Flow around a Statically Loaded Tire. *Symmetry* **2021**, *13*, 1319. https://doi.org/10.3390/sym13081319

Academic Editor: Juan Luis García Guirao

Received: 22 June 2021
Accepted: 21 July 2021
Published: 22 July 2021



## 1. Introduction

Due to global warming, an increasing number of steps have been taken by vehicle manufacturers and governments to reduce $CO_2$ emissions. Decreasing the aerodynamic drag of automobiles is regarded as an effective measure to reduce $CO_2$ emissions. A 5% reduction in automotive aerodynamic drag will result in a 1.5 g/km reduction in $CO_2$ emissions [1]. To protect the environment from pollution, electric vehicles (EVs) have become a major trend in the car industry. Compared with the powertrain energy losses of a traditional internal combustion engine (ICE) vehicle, the losses for an EV are smaller. However, the ratio of the aerodynamic loss to the total energy loss of an EV is about 4.4 times higher than that of ICE vehicles [2]. Therefore, aerodynamic drag minimization is a priority during the vehicle development process. However, it cannot be ignored that the drag contribution of the tire and wheel lies in the range of 15 to 25% of the vehicle aerodynamic drag [3]. The aerodynamic drag of the tire and wheel have been found to have a direct relationship with the flow around the wheel [4]. To understand the flow characteristics around the tire, a wind tunnel test was conducted by Fackrell, and the aerodynamic force of the tire was obtained by integrating the static surface pressure [5]. To analyze the influence of the tire shape on aerodynamic drag, Landström et al. [6] conducted wind tunnel tests on two 205/55R16 tires, with these two tires having a 10 mm width difference, and the results revealed that the aerodynamic drag increased by about 2% for the wider tire. Wittmeier [7] analyzed the effects of tire shoulder geometries on the flow field and suggested that the tire aerodynamic performance can be improved by smoothening the shoulder profile. Hobeika et al. [8] pointed out that the rain grooves have a positive effect on reducing tire aerodynamic drag by decreasing the pressure difference at both ends of the tire contact area. The lateral grooves have a negative influence on decreasing tire aerodynamic drag.

The wind tunnel test requires considerable space and an expensive test facility; for example, the particle image velocimetry (PIV) or the high-speed camera is selected to capture velocity field [9,10], but because of the complex test conditions, it is difficult to conduct aerodynamics research in the academic and industrial community. To overcome the disadvantage of the wind tunnel test, numerical simulation with computational fluid dynamics (CFD) code has been approved as one of the efficient and useful tools for studying tire aerodynamics [11]. It is found that CFD simulation results are consistent with the experimental measurements, and it has been approved as an effective and accurate method to evaluate the flow characteristics around a tire by both the German Research Association of Automotive Technology (FAT) [12,13] and the Society of Automotive Engineers (SAE) [14]. It can be not ignored that the contact shape between tire and road, or the tire rotation model, has significant influences on the CFD simulation accuracy [15]. Moreover, the turbulence model also plays an important role in the computational accuracy [16], and no one turbulence model can be universally applied to all fluid simulations. It is reported that the turbulence models applied in the tire or wheel aerodynamics studies include Reynolds-averaged Navier–Stokes (RANS) equations, large-eddy simulation (LES), and detached eddy simulation (DES). Axon et al. [11] used the steady RANS method to analyze the flow field around a rotation wheel, and the simulation results of aerodynamic drag coefficient had a relative error of about 3.8% compared with the experimental results obtained by Fackrell [5]. Diasinos studied the effects of the Spalart Allmaras (SA), shear stress transport (SST) and realizable k-ε model on flow over a tire and pointed out that the SST model yielded almost identical plots [17]. Although the steady RANS method provides some information about the complex flow phenomena, the main disadvantage, however, is that airflow states are not steady, and it is virtually impossible to obtain flow details with the RANS method. Therefore, more accurate methods are recommended by LES or DES to analyze the flow characteristics around a tire or wheel [18].

LES, in which the smaller-scale features are modeled and the large range of scales contained in the flow is explicitly resolved, does not decompose the aerodynamic components into the mean and fluctuation section; thus, it holds advantages over traditional approaches such as time-averaged model analysis. Huang et al. [19] studied the aerodynamic characteristics of a nonpneumatic tire by using LES. The simulation results of pressure coefficients agreed with the experimental results except for the results for tire contact area. Ramachandran and Doig [20] investigated the flow field around an exposed wheel by using the steady RANS, unsteady RANS, and LES methods. They pointed out that, compared with the RANS method, LES can present a higher number of physical flow features that are expected to occur in real life. However, a critical problem for LES is the cost required to refine the boundary layer mesh and resolve the near-wall region. DES model is a hybrid method that combines RANS and LES. In other words, the DES uses the RANS method for the near-wall regions and uses LES for the remainder of the flow far away from the boundaries. Salati [21] used DES to investigate and predict the flow characteristics and pointed out DES can provide a good surface static pressure correlation by using Fackrell's experimental work. Collectively, the work presented by Dassanayake et al. [22] concluded that LES or DES can capture flow vortices around the isolated wheel that were not apparent by using unsteady RANS simulations, and it pointed out that LES is more computationally expensive than DES in the simulation process.

It is certain that CFD has enormous advantages in studying the flow field characteristics of tires. However, the tire models are highly simplified. For example, an isolated simplified smooth tire without patterns and with no deformation was investigated [17].

Actually, the deformation profile and contact shape of a loaded tire will have a direct effect on the airflow field over the tire. It is fact that there are some differences between the flow around an isolated tire and that of a tire mounted in a car; however, due to the open zones under the car body that lead to similar flow field characteristics near the ground, the flow field near the isolated tire contact patch is very similar to that of the tire mounted in a car (e.g., the separated flow and vortices around tire) [23]. When the airflow passes through the underbody, the complex tread patterns and the deformation sidewall shape of the partially loaded tire, which is out of the wheelhouse and exposed to the free airflow between the underbody and the ground, can easily disturb the air motion around the tire and result in flow separation and vortex formation. It can be illustrated that the different selections of turbulence models will have a significant impact on the prediction results of tire aerodynamics.

Therefore, the aim of the paper is to determine the most suitable turbulence approach to study the aerodynamics of a tire with a complex tread pattern. This is performed by comparing the performances of three turbulence approaches, k-ω SST, LES, and DES, on the lower section of a cut 185/65 tire, which is statically loaded. The evaluation is made in terms of surface pressure and flow field. Firstly, the outer profile deformation features were obtained using finite element analysis (FEA); then, the deformed tire geometric model was rebuilt by three-dimensional (3D) printing with a 1:1 scale ratio, and the surface pressure coefficient was tested in the wind tunnel. Then, the comparisons of the surface pressure and flow around the partially statically loaded tire using SST, LES, and DES were analyzed and discussed to determine the more suitable turbulence model for investigating tire aerodynamics. The research results will provide a reference for developing the low-aerodynamic-drag tire design.

## 2. Geometry Model of the Loaded Tire

A passenger car radial (PCR) tire 185/65 R14 was selected in this study. To reflect the influence of the deformable profile on the tire aerodynamics, a finite element model of a static tire with the inflation pressure of 241.3 kPa and the load of 4000 N was established. The detailed modeling process is described in the work by Zhou et al. [24]. A radial deformation test was conducted to test the tire model, as shown in Figure 1a. A comparison between the radial deformation simulation results and experimental tests is presented in Figure 1b. Taking the vertical stiffness as an object, the relative error between simulation and test was 6.08%. Besides, the largest deformations in tire section width were 205.2 and 203.5 mm for the experiment and simulation, with a difference of 2%. It can be illustrated that the proposed tire finite element model is accurate enough to reproduce profile deformation. When a tire is mounted on the car, the distance from the automobile chassis to the ground is approximately 150 mm; thus, a partially loaded tire geometric model with a height of 150 mm was built. The outer profile and tread groove deform easily under the vertical loads acting on the actual tire, and these deformation features have important influences on tire aerodynamics. Therefore, the effects of the loaded tire deformation on tire aerodynamics cannot be ignored. To represent the tire deformable profile in the wind tunnel test, a solid geometry model was reproduced using 3D printing technology with a 1:1 scale ratio, and the sizes and deformation features are showed in Figure 2. It can be seen that the grooves are squeezed and the contact patch is the plane surface.

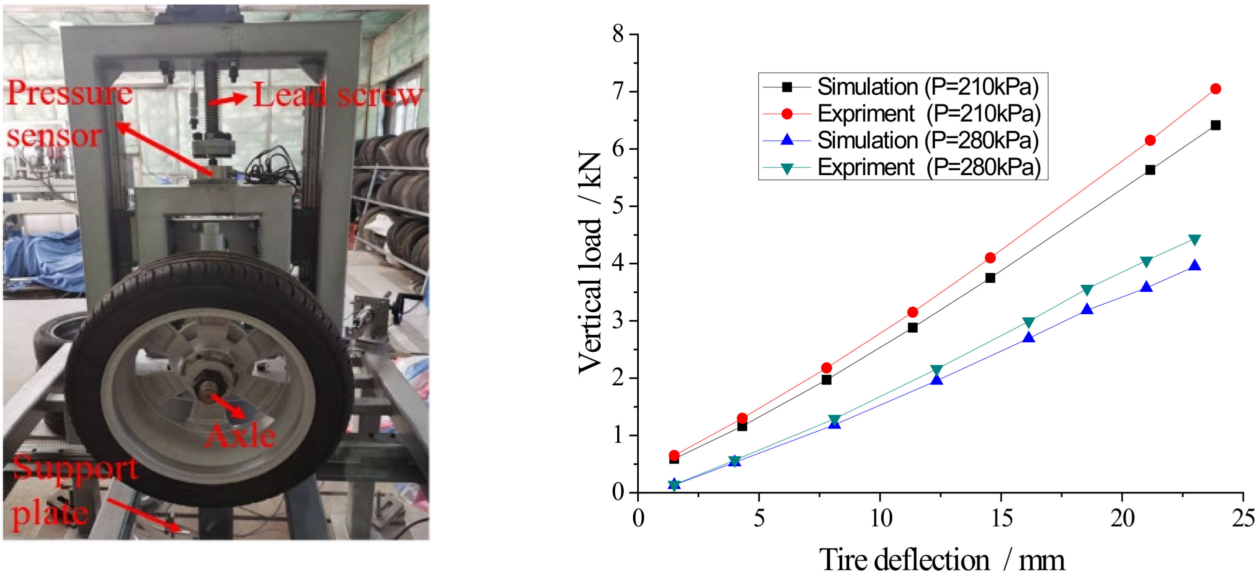


(**a**) (**b**)

**Figure 1.** Test and simulation for tire stiffness. (**a**) Stiffness test; (**b**) stiffness simulation.

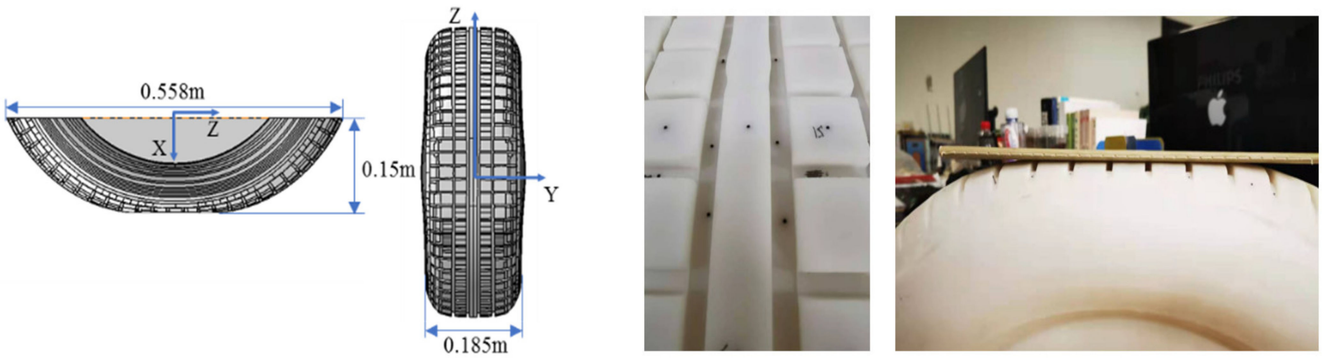


(**a**) (**b**)

**Figure 2.** Tire model sizes and deformations. (**a**) Model sizes; (**b**) deformation features.

## 3. Wind Tunnel Experiment

The wind tunnel experiment for the tire surface coefficient was conducted at Yangzhou University. The wind tunnel includes low-speed and high-speed test sections, and the wind speed range is from 0 to 25 m/s. The tire model was braced by a plate to reduce the influence of the unstable flow near the bottom on tire aerodynamics. The plate was above the bottom with a height of 1 m, and the tire model was fixed on the central line of the plate. Figure 3 shows the experimental devices and sizes employed in the wind tunnel.

The surface pressure coefficients were recorded by using an electronic pressure transducer, which includes 2 modules and 128 channels, as shown in Figure 4. There are 15 lateral sections and 4 longitudinal sections in the tire model; each odd lateral section has 7 measuring points, each even lateral section has 6 measuring points, and each longitudinal section has 9 measuring points [25]. The detailed arrangement of pressure measuring points is presented in Figure 5. Due to the 128 channels and the limit of 14 intersection points between the lateral sections and the longitudinal sections, there were 114 pressure measuring points in total.

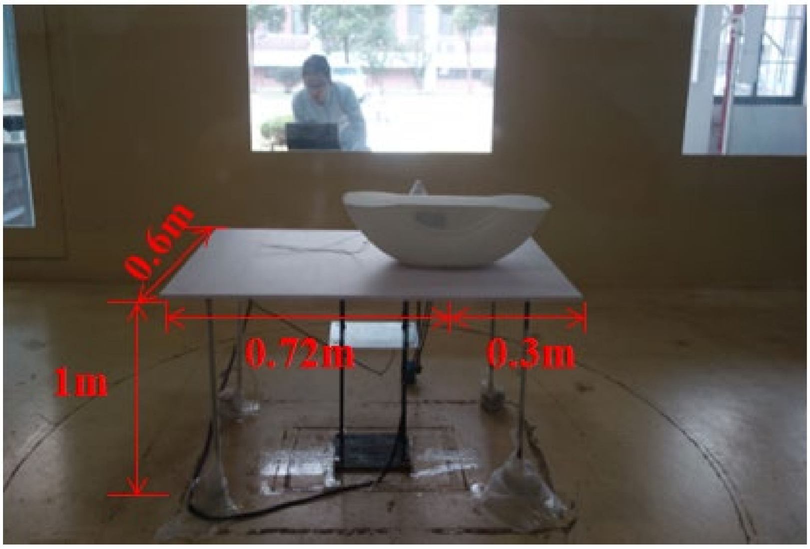


**Figure 3.** Tire installed in wind tunnel.

(**a**) (**b**)

**Figure 4.** Pressure measuring. (**a**) Pressure transducer; (**b**) pressure measurement points.

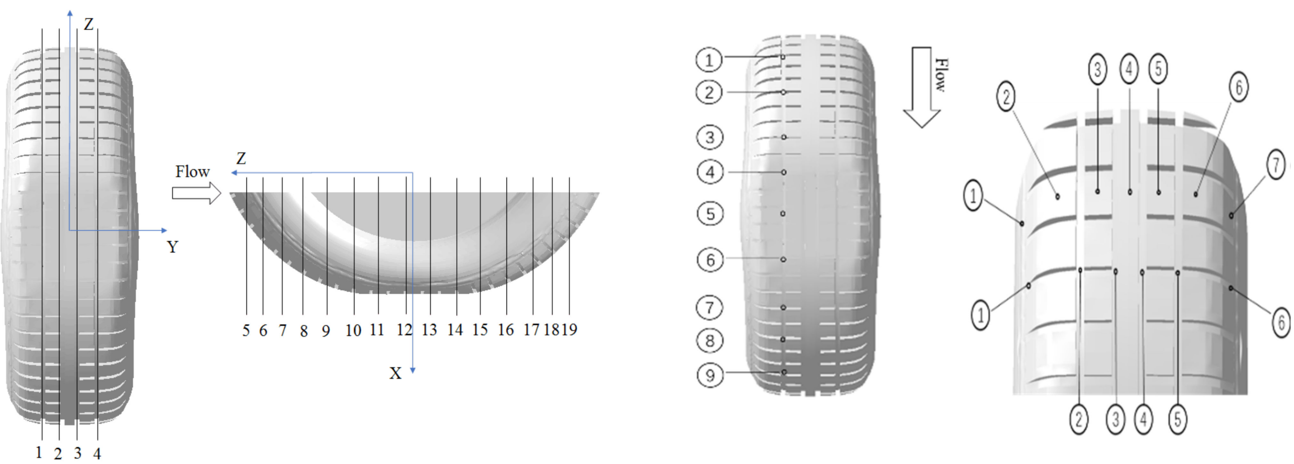


(**a**) (**b**)

**Figure 5.** Tire sections and pressure measuring points. (**a**) Section positions; (**b**) point position distribution.

## 4. Numerical Simulation Model

### *4.1. Turbulence Model*

Compared with the unsteady analysis of LES or DES, the RANS turbulence model has the advantage of the capacity to obtain relatively acquire time-averaged results. The SST k-ω model is one of the popular two-equation RANS models; it accounts for the transport of the turbulent shear stress and provides highly exact predictions of the onset and the amount of flow separation under adverse pressure gradients. The detailed equations of the SST k-ω model are presented in [26].

LES model directly calculates large-scale eddies, whereas only small-scale eddies are modeled by the subgrid-scale model. Thus, the LES model can provide higher accuracy than the typical RANS model. A comprehensive introduction of LES equations is presented in a study by Liu et al. [27].

The improved delayed DES (IDDES), which originates from the DES method, utilizes a hybrid RANS–LES approach that resolves turbulence motion using LES only in the field of a large or detached separation region and models turbulence using RANS in almost the whole boundary. The complete transport equations of IDDES and the SST-IDDES model are provided in [28].

### *4.2. Computational Domain and Boundaries*

The outline profile of the statically loaded tire was extracted using the 3D Free-Curved Surface in CATIA Software, and the partially loaded tire model was obtained by a cutting plane with the height of 150 mm. Then, using the Boolean operator "subtract", the tire model was removed from the wind tunnel model. The length, width, and height of the computational domain are 7, 1.5, and 3 m, respectively, and the refinement box and the detailed boundary settings are presented in Figure 6. In order to improve the mesh quality near the contact patch, there is a convex plate with 1 mm height at both ends of the contact zone in the middle plane, as shown in Figure 7. The computational domain setting is similar to the wind tunnel test setting. The outlet boundary is zero-pressure; the tire, table, and ground are nonslip wall conditions; and the inlet velocity is 15 m/s. The top surface and sides are set as symmetric boundary conditions.

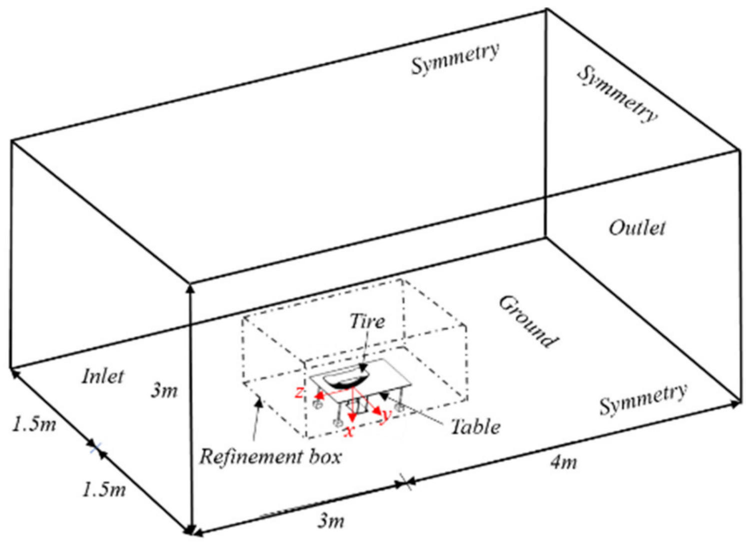


**Figure 6.** Computational domain and boundaries.

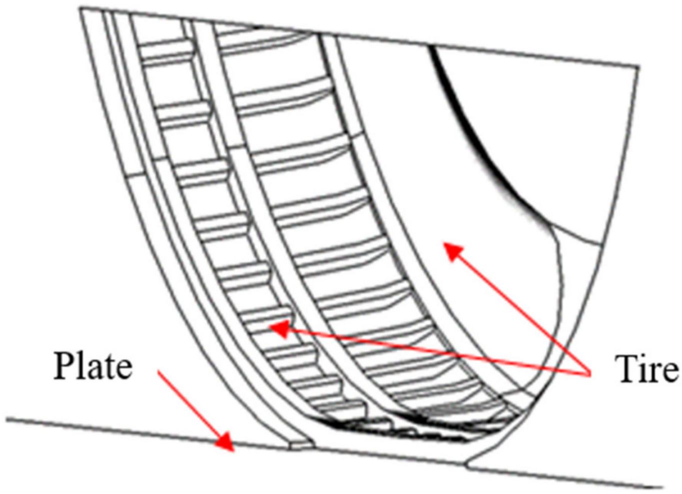


**Figure 7.** Locally enlarged view of the tire contact zone.

### 4.3. Numerical Method

The simulation analysis was conducted according to the flow reaching an acceptable convergence that was judged by two criteria. Firstly, a steady-state calculation was conducted until the numerical calculation satisfied full convergence conditions in which the calculated residuals of all transported quantities dropped by at least three orders of magnitude. Secondly, the averaged drag coefficient over the last 500 iterations needed to not show obvious fluctuation. Then, the next unsteady simulation was conducted based on the initial conditions of the steady numerical results. During the unsteady simulation, the flow field characteristics were predicted using the LES and IDDES.

The temporal terms for LES and IDDES were discretized using a second-order backward implicit scheme. A second-order central differencing scheme was selected for the source and diffusion terms. The convection terms of the momentum and turbulence equations were discretized using a second-order upwind scheme for the RANS and IDDES models. However, a bounded central differencing scheme was implemented for the LES model. The semi-implicit method for pressure-linked equations (SIMPLE) was employed for the pressure–velocity decoupling method in the RANS simulation. The pressure-interpolated splitting of operator (PISO) algorithm was chosen for LES and IDDES.

In the unsteady simulation of LES and IDDES, the step time $\Delta t$ was determined as 0.0001 s, which can provide corresponding mean and maximum Courant–Friedrichs–Lewy (CFL) numbers of 0.001 and 2, respectively. The total number of iterative steps was 20,000, which leads to 2 s of flow time. The last 8000 steps were used to compute the average results of velocity. A few cells (less than 30,000) of the computational domain had CFL numbers larger than 1. Compared to the million cells, these cells almost had no significant effect on the flow field. The double-precision mode of ANSYS Fluent was used to conduct all the numerical simulations of different models.

### 4.4. Computational Mesh

The computational domain was discretized using the HyperMesh software to generate the cells. In order to really reflect the boundary layer flow over the tire model, the first layer mesh thickness normal to the tire surface was 0.05 mm, the expansion ratio was 1.2, and the boundary region had 10 layers. The coarse, medium, and fine meshes consisted of 4.2, 8.8, and 14.5 million cells, respectively. The sizes of tire surface cells in the three different meshes models were 3, 1, and 0.5 mm, and the maximum mesh sizes of the tire surface were 8, 5, and 3 mm, respectively. The details of the three computational meshes are outlined in Table 1. The locally enlarged view of the medium mesh is shown in Figure 8.

**Table 1.** Mesh sensitivity analysis using IDDES model.

| Mesh Type | Surface Cell Size | Thickness of First Boundary Layer | Number of Boundary Layers | Number of Total Cells | Time of 100 Iterations | Drag Coefficients |
|---|---|---|---|---|---|---|
| Coarse | 3~8 mm | 0.05 mm | 10 | 4.2 Million | 249.9 s | 0.407 |
| Medium | 1~5 mm | 0.05 mm | 10 | 8.8 Million | 534.4 s | 0.395 |
| Fine | 0.5~3 mm | 0.05 mm | 10 | 14.5 Million | 878.5 s | 0.394 |

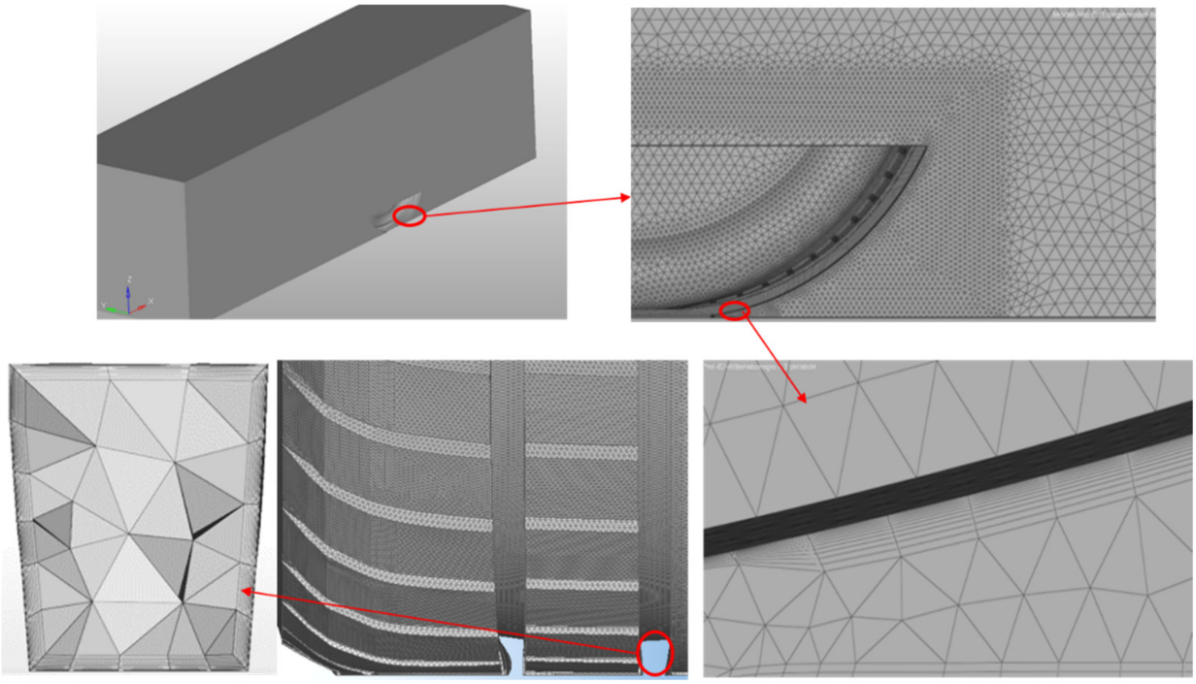

**Figure 8.** The locally enlarged view of medium mesh on the middle plane of the tire model.

### *4.5. Mesh Sensitivity*

For the mesh independence, the IDDES model was chosen for numerical simulation. The drag coefficients of the tire are also shown in Table 1. When the number of meshes increased from 8.8 million to 14.5 million, the relative difference in drag resistance was 0.001. Due to the LES and IDDES models belonging to the scale resolution model, the calculation requirement of LES and DES models is that the first layer mesh thickness normal to tire surface should be close to the values of $y^+$ less than 1. The $y^+$ values of the LES and IDDES models obtained by using the medium mesh are presented in Figure 9, and it shows that the $y^+$ values of LES and IDDES models were mostly less than 1, and the medium quality can meet calculation requirements.

The surface pressure coefficient $C_p$ is defined as

$$C_p = \frac{p_i - p_r}{0.5\rho U_r^2} \tag{1}$$

where $U_r$ is the airflow speed, $P_i$ and $P_r$ are the measured mean pressure and the reference pressure, respectively, and $\rho$ is the air density. In this experiment, the reference pressure $P_r$ is considered static pressure 101,325 Pa.

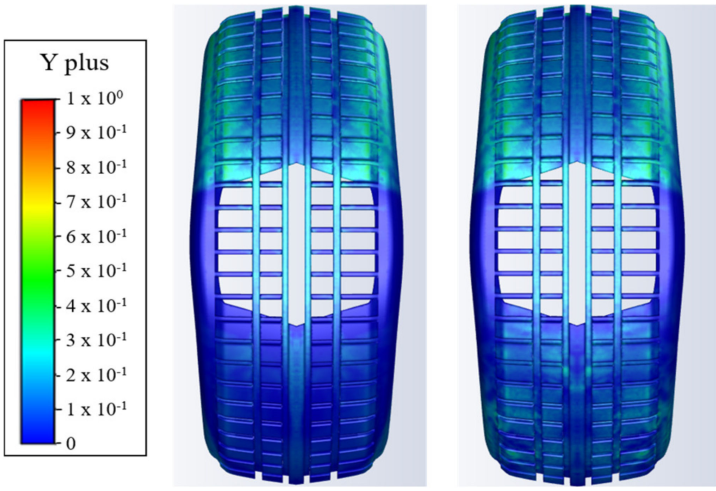


**Figure 9.** The surface $y^+$ values of the tire using different models (left, LES; right, IDDES).

Two sections for mesh sensitivity were section 1 and section 9; one is located in the longitudinal direction and the other is located in the lateral direction. The surface pressure coefficients $C_p$ on sections 1 and 9 obtained using the IDDES with different meshes are compared and shown in Figure 10. It can be seen that the three mesh parameters show similar trends and have no impact on the surface pressure coefficient of the front contact patch. However, they have a large influence on the pressure coefficient of the contact patch and the rear surface, as shown in Figure 10a. Taking the average relative error as a criterion, the average relative errors of different measuring points using different mesh types in section 1 were 14.5% using coarse, 11.6% using medium, and 10.4% using fine. The $C_p$ value of the fine mesh was higher than that of the test, and the $C_p$ values of the medium and coarse meshes were lower than that of the test. The medium mesh could accurately predict the surface pressure coefficient of the longitudinal section 1, except for the contact patch. The reason might be that the tread groove deformations were complex and irregular in the contact patch; slight differences were observed between the CFD simulation and the real deformations used in the wind tunnel test. Figure 10b shows that the mesh sizes almost have no effect on the surface pressure coefficient of section 9. Based on consideration of the iteration time and drag coefficients mentioned above, the medium mesh was selected for the following simulations.

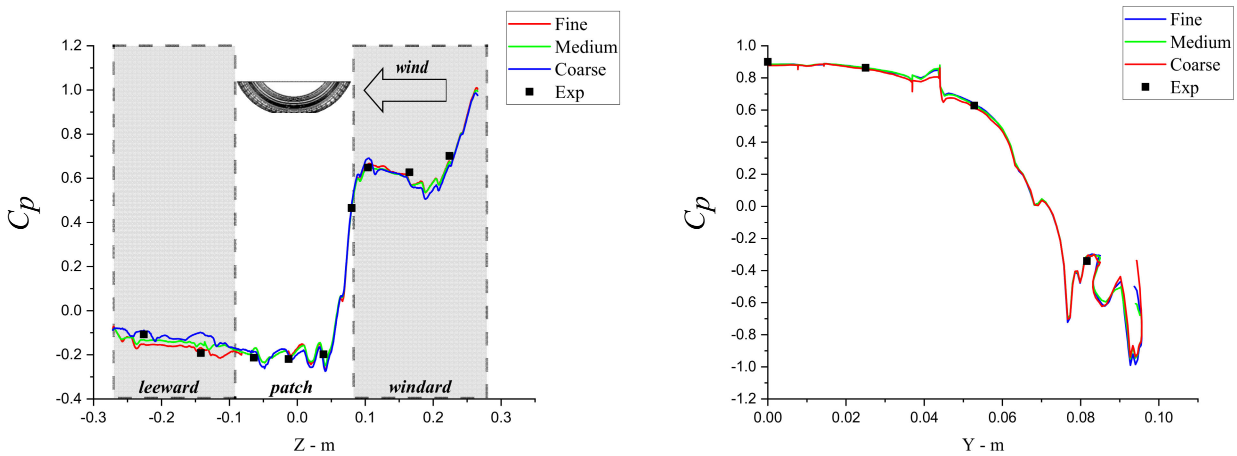


(**a**) (**b**)

**Figure 10.** Pressure coefficients along two sections using IDDES for different meshes. (**a**) Section 1 (y = 0.011 m); (**b**) section 9 (z = 0.125 m).

## 5. Results and Discussion

### *5.1. Comparisons of Surface Pressure Coefficients*

Figure 11 presents the values of $C_p$ obtained using SST, LES, and DES along sections 1 and 2. It can be seen that the turbulence models have different effects on the $C_p$ on the windward surface, contact patch, and leeward face, and a high $C_p$ is observed on the windward surface. The $C_p$ values of both SST and LES were obviously fluctuating on the leeward face, and the $C_p$ value of DES was relatively flat. Figure 11a shows that the LES model predicted a significantly smaller $C_p$ value than the DES and SST models in the windward zone, and the $C_p$ values obtained using the SST and LES models in the leeward zone were higher and lower than those obtained by experimentation, respectively. However, the $C_p$ value obtained using the DES model was similar to that obtained by experimentation. Taking the average relative error as the criterion, the average relative errors of different measuring points in section 1 were 22.4% using SST, 20.9% using LES, and 14.8% using DES. The $C_p$ values had the same trend on the longitudinal section 2. However, the three models also exhibited fluctuations in the leeward zone, as shown in Figure 11b. The difference between the results of the three models and the experimental results in the longitudinal section 2 is similar to that for the longitudinal section 1. The reason for this difference may be that the outlets in the leeward zone have air jets with higher speeds, and this results in a separated flow and countertrading vortices, which was discussed by McManus and Zhang [18]. Therefore, in a subsequent analysis, the flow field characteristics must be considered.

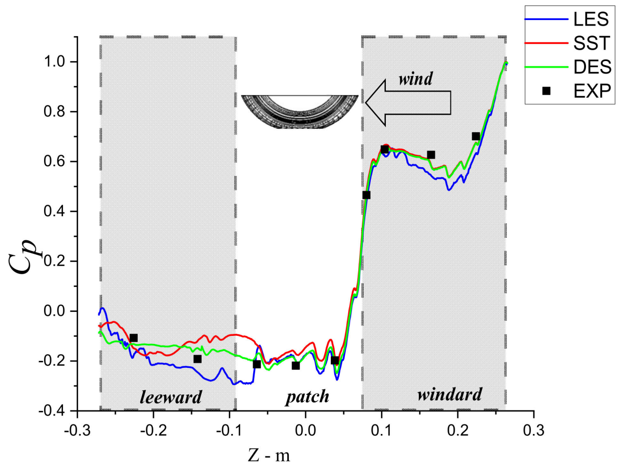


(**a**)

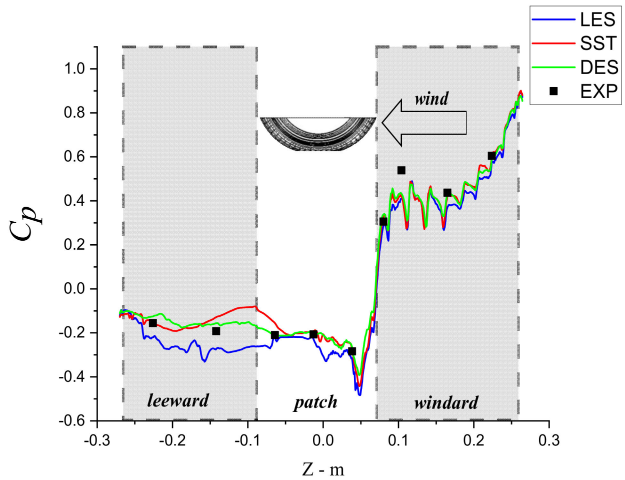


(**b**)

**Figure 11.** Pressure coefficients $C_p$ obtained using three models along longitudinal sections. (**a**) Section 1 (y = 0.011 m); (**b**) section 2 (y = 0.0387 m).

As the tread on the tire is symmetric, the surface pressure coefficient $C_p$ in half of the lateral sections was used in the analysis. Figure 12 displays a comparison of the $C_p$ values in different lateral sections in the windward surface. The highest $C_p$ value exists at the center of the tread (Y = 0 m), and the lowest $C_p$ value exists at the sidewall. The tendencies of the simulated $C_p$ values of the three models are almost consistent with the experimental result, and the average deviation is small and within 3.5%. However, the simulated $C_p$ value obtained using the LES model in section 7 was slightly lower than the experimental value obtained near the center of the tread.

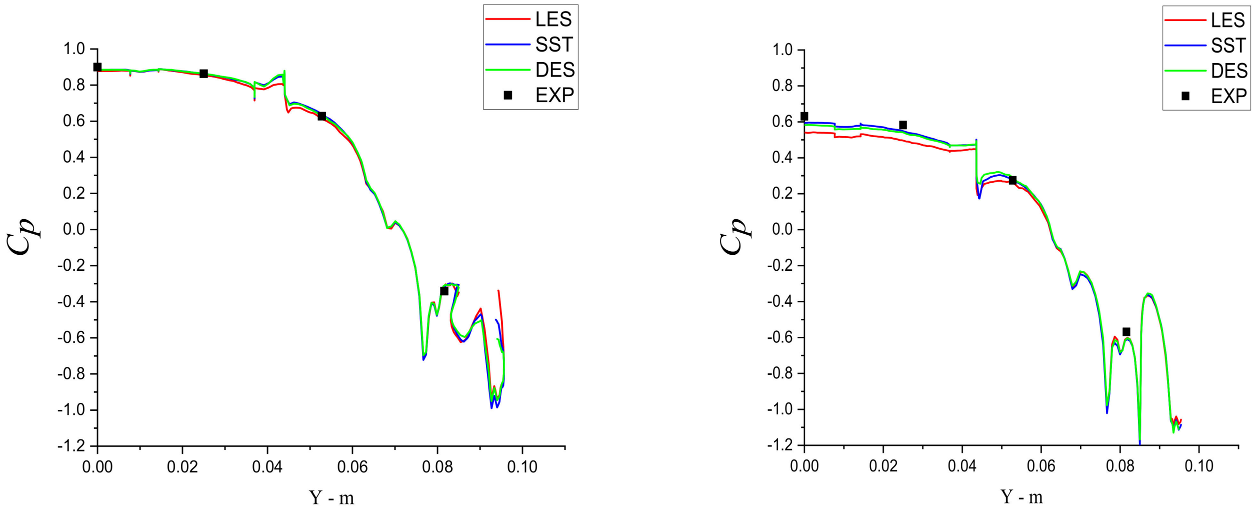


(**a**) (**b**)

**Figure 12.** Pressure coefficients on lateral sections in the windward surface. (**a**) Section 5 (z = 0.244 m); (**b**) section 7 (z = 0.19 m).

Figure 13 displays the difference between the predicted and the wind tunnel test $C_p$ values of different transverse sections in the leeward zone. The $C_p$ values obtained using the LES and DES model were lower than those obtained by experimentation. Moreover, the $C_p$ values obtained using SST models were higher than those obtained by experimentation. It can be seen that the $C_p$ value obtained through the wind tunnel test decreased with the distance from the center, the LES and DES presented a similar trend of pressure change; however, the SST model presented relatively steady flow near the sidewall and cannot reflect this decreasing tendency. The average relative errors of different measuring points in sections 14 and 16 were 24.5% using SST, 11.5% using LES, and 15.6% using DES. For a comprehensive analysis of the effects of turbulence models on surface pressure coefficients $C_p$, it is necessary to analyze the differences in flow fields obtained using different turbulence models to determine the more suitable turbulence model to study tire aerodynamics.

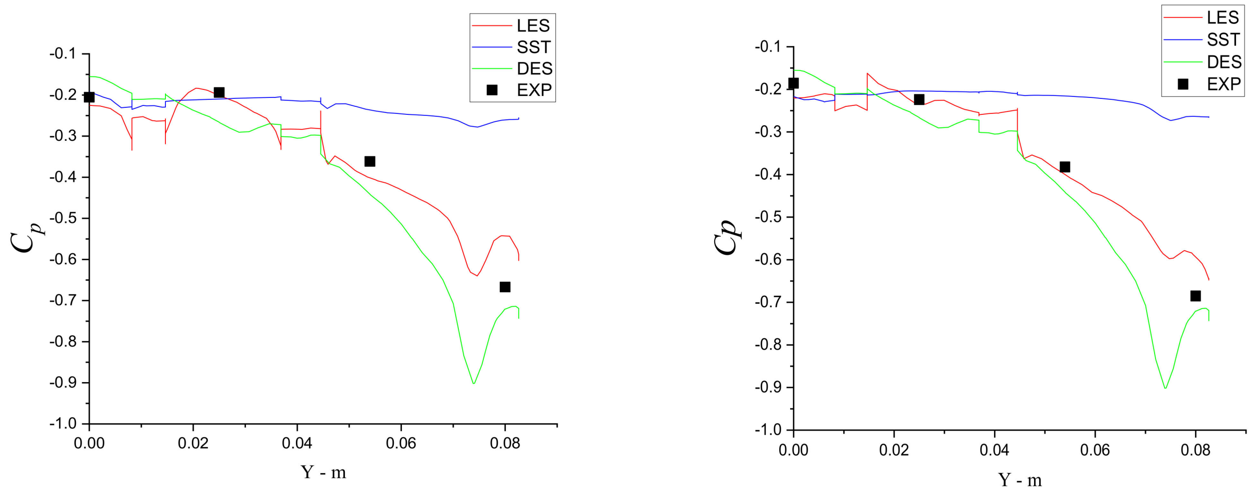


(**a**) (**b**)

**Figure 13.** Pressure coefficients on lateral sections in the leeward surface. (**a**) Section 14 (z = −0.09 m); (**b**) section 16 (z = −0.16 m).

*5.2. Comparisons of Flow Field Characteristics*

The flow field characteristic in a horizontal plane 0.002 m above the bottom surface was analyzed. Figure 14 displays the average velocity distribution in the horizontal plane for the three models. The turbulence models have a noticeable effect on the velocity fields. There are few differences at the windward surface, and even the flow separations are similar to an extent. The differences in velocity are concentrated mainly in the leeward zone. The SST and LES predicted a typical shear layer, with the velocity gradient perpendicular to the flow direction. Moreover, the regions obtained using the SST and LES were dominated by large-scale vortices and nonuniform velocity distribution. Differences between the three turbulence models are seen in the vortex fields (Figure 15), where SST shows the vortices only around the tire contact area, while the distinctive vortices using LES and DES appear in the wake region.

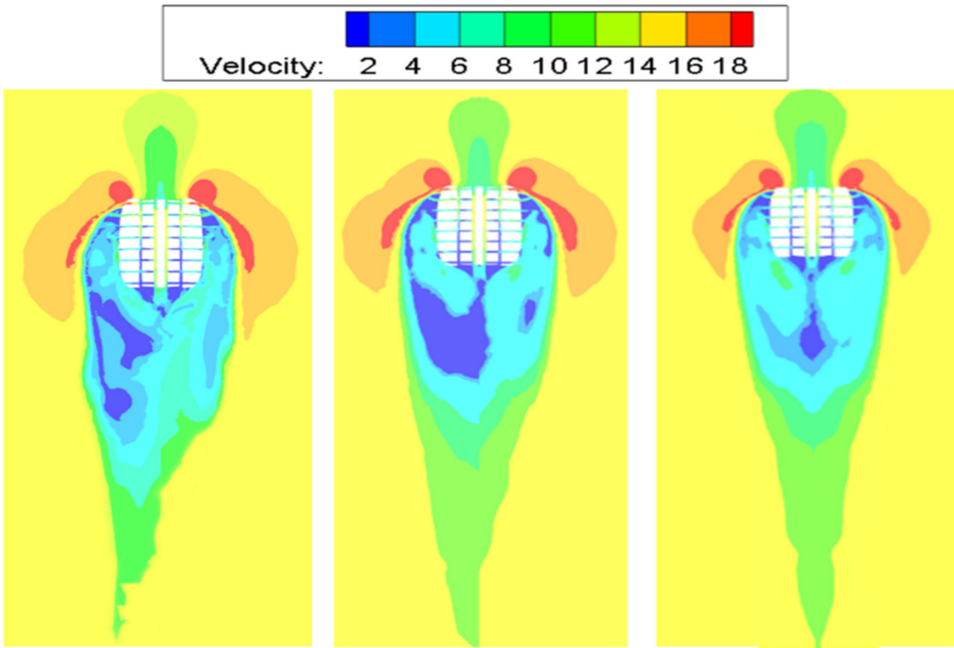


**Figure 14.** Average velocity fields using different models in a horizontal plane.

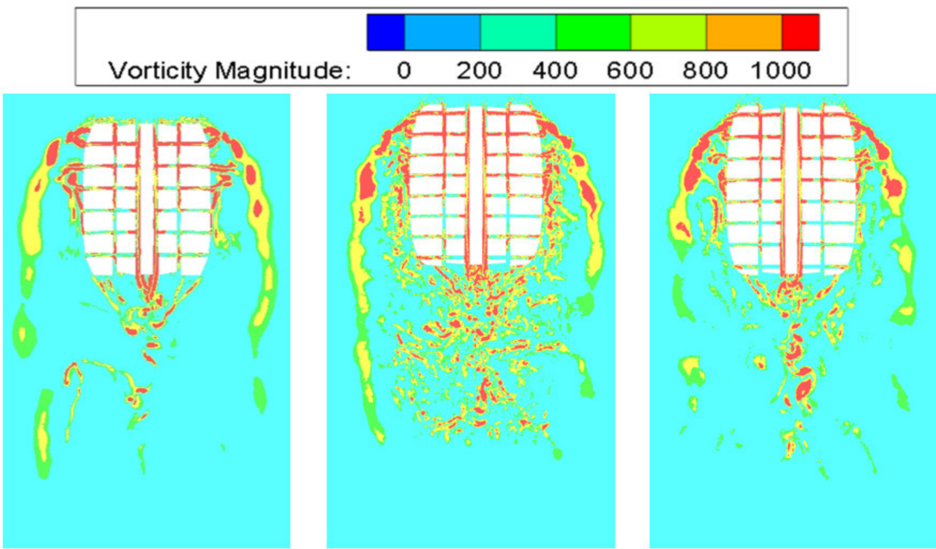


**Figure 15.** Vortex field using different models in a horizontal plane.

In general, the flow separation and the complex flow structure occur around the tire due to geometric singularities introduced by the tread pattern. Because of the adverse effects on a tire, the flow stagnates at points near the front of the tire contact patch. The flow accelerates from the stagnation points and reaches the highest value at both sides of the sidewall. However, the flow velocity has a sudden change on the leeward surface, that is, a negative pressure region on the leeward surface. The phenomenon of the negative pressure region was in agreement with other studies published by Schnepf et al. [15]. According to the average velocity distribution illustrated in Figure 14, the biggest region of the minimum velocity of the three turbulence models is found for LES, the second is for SST and the last is for DES. This implies that the LES provides the most noticeable negative pressure region, followed by the SST and finally the DES.

Figure 16 displays the flow streamlines obtained using three models. The flow field on the leeward surface is greatly different. The streamline has changed significantly, and the characteristics of shape, size, number, and location of the wake vortex are significantly different. The SST model can capture a few vortices near the ground that have a large diameter, while the LES and DES models can capture smaller diameter vortices. A study by Dassanayake et al. [22] proposed that the RANS simulation cannot present the counter-rotating vortices and shedding vortices on the leeward surface that are presented by the LES and DES models. This is due to the differences in different turbulence models in the numerical calculations for the flow separation caused by the tire. Because the size of vortices is very sensitive to the viscosity coefficient, the viscosity coefficient of different turbulence models may differ several times, which is also the reason for the difference in calculated vortices. According to the analysis result of $C_p$ of the tire on the leeward surface, the main reason for the difference in $C_p$ values obtained using different models is that the flow field characteristics are quite different in the three models.

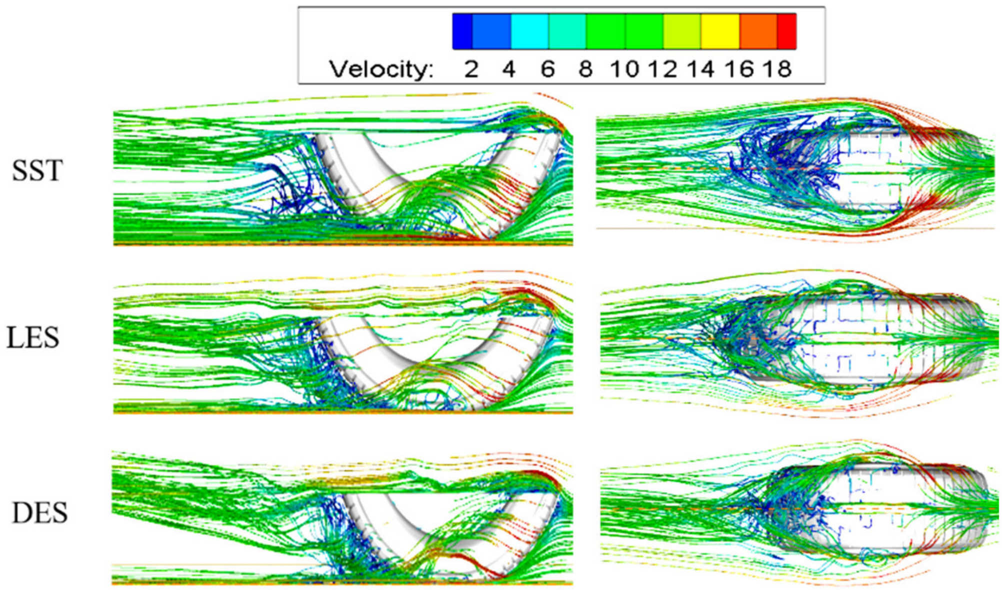


**Figure 16.** Streamlines of the flow field around tire colored by velocity.

Figure 17 shows the z-velocity distribution of different cross-sections along the flow direction. It can be seen that the turbulence models have noticeable effects on the velocity field. The airflow vortex is easily generated at the sidewall and wake, which leads to an increase in the flow energy consumption. Compared with the SST model, the LES and DES models can capture the detailed flow characteristics in the flow direction. Compared with the DES model, the relative velocity using SST and LES appears around the tire sidewall at the same position (there is less separation at z = −0.2 m), which means that the flow separation would take place earlier. With the increase in the distance from the contact patch, the airflow causes the development of the tire wakes (z = −0.3 m, z = −0.4 m), and the range of the vortex becomes small. Figure 18 presents the comparison results of streamlines among the three turbulent models. It can be seen that the SST simulation is not able to capture the detailed vortices, while LES and DES can capture similar wake structures; the differences mainly focus on the positions of vortices. Compared with the experimental results of the vortices positions conducted by Parfett [29], DES is more advantageous than LES to capture the two much smaller structures near the ground. A reason for this difference is that the tire used in this study has complex tread patterns, and the experimental tire does not, and these differences would result in flow field change consistent with the conclusions from Hobeika that tread grooves have a significant effect on the flow field around a tire [8].

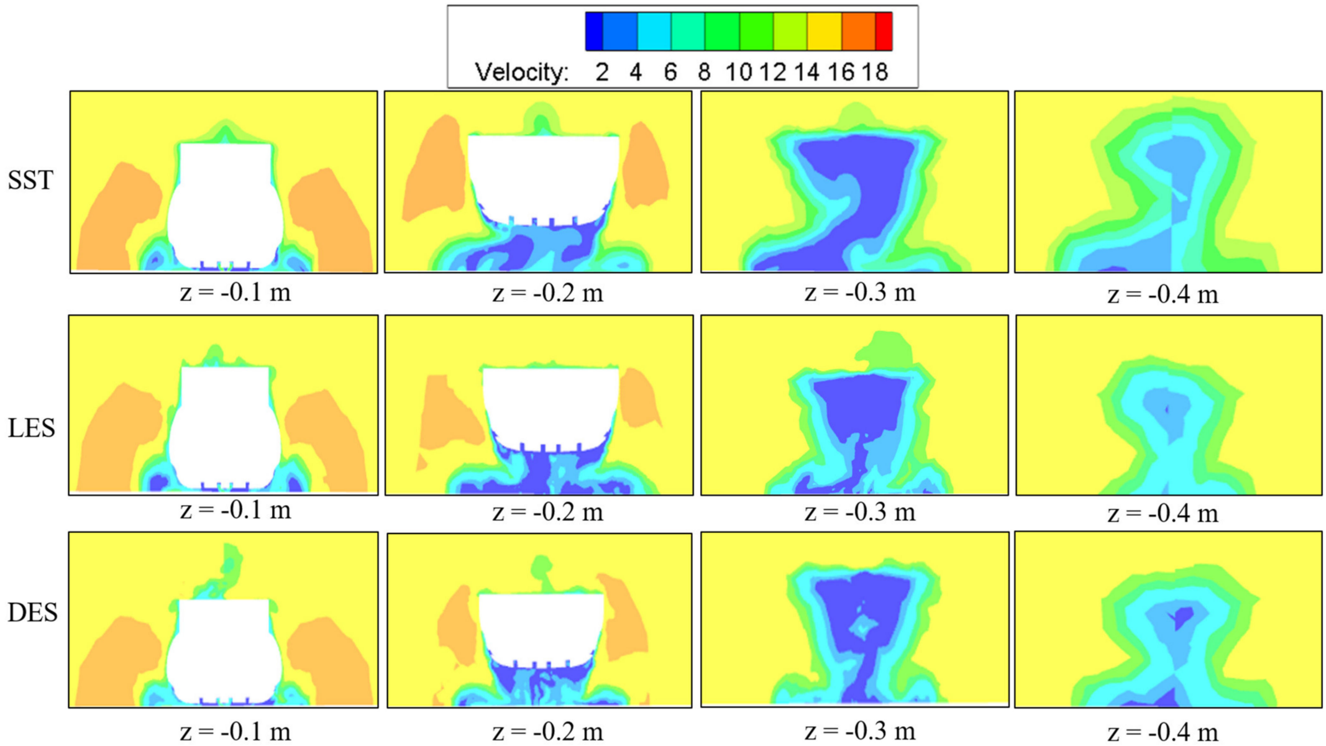


**Figure 17.** Z-velocity distribution of different cross-sections along the flow direction.

Dubief and Delcayre [30] proposed the $Q$ criterion as a method for identifying the vertical coherent structure. The size and strength of flow vortices can be better visualized with the help of the $Q$ criterion, as shown in Equations (2)–(4):

$$S_{ij} = \frac{1}{2}\left(\frac{\partial u_i}{\partial x_j} - \frac{\partial u_j}{\partial x_i}\right) \quad (2)$$

$$\Omega_{ij} = \frac{1}{2}\left(\frac{\partial u_i}{\partial x_j} + \frac{\partial u_j}{\partial x_i}\right) \quad (3)$$

$$Q = \frac{1}{2}\left(\left\|\Omega^2\right\| - \|S\|^2\right) \quad (4)$$

where $S_{ij}$ is the rate of strain tensor and $\Omega_{ij}$ is vorticity; they are the antisymmetric and symmetric parts of the velocity gradient, respectively. Thus, the quantity $Q$ represents the balance between the rate of vorticity $\Omega^2 = \Omega_{ij}\Omega_{ij}$ and the rate of strain $S^2 = S_{ij}S_{ij}$, which is the local balance between the shear strain rate and magnitude of vortices. In the present study, the iso-surfaces of the $Q$ criterion are used to visualize these flow structures.

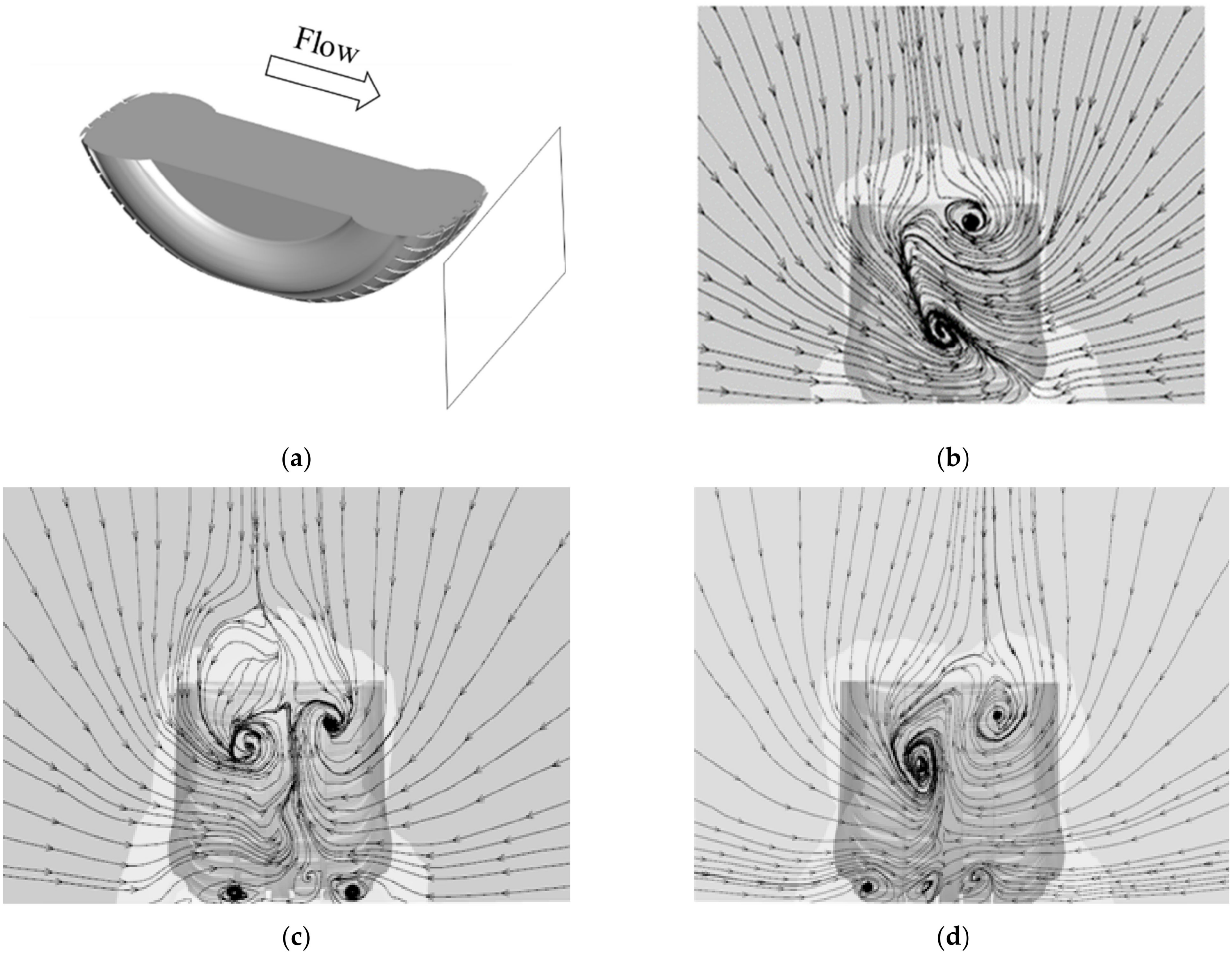


**Figure 18.** Comparisons of streamlines between experiment and simulations. (**a**) Measurement planes at z = −0.35 m; (**b**) SST model; (**c**) LES model; (**d**) DES model.

Figure 19 illustrates instantaneous iso-surfaces of $Q$ criterion ($Q$ = 4000) colored using the velocity component on the leeward surface. The flow separates from the tire near the bottom of the contact patch, which appears in all three turbulence models, and the flow separation emerges at the sidewall; these phenomena were also presented in Wäschle's results [22]. Since the tire's outer profile is not streamlined, the vortex is caused by the flow separation. When placing an isolated tire on the ground, the flow near the ground is forced outwards on each side of tire. This phenomenon is called the jetting effect, and there are four types of flow vortex around the isolated tire, the jetting vortex ①, the horseshoe vortex ⑤, the C-shoulder vortex ③, and the horseshoe vortex behind the tire ②. Although there are major differences between the flow around an isolated tire and that of a tire mounted in a car, the open zones under the car body would lead to similar flow field characteristics near the ground. Concentrating on the lower portion of the tire mounted in the car shown in Figure 19a, the jetting vortex ① and the horseshoe vortex ② around the isolated partially loaded tire model appear around the tire contact patch when using LES and DES, and the horseshoe vortex ② does not appear when using SST. However, the number of wake vortices obtained using LES is larger than that obtained using DES, and it can be seen from the differences in Figure 16 that there are many small vortices in the leeward zone. The change in the vortex structures causes energy dissipation and pressure fluctuation [31]. The vortex structures obtained using three turbulence models were significantly different on the leeward surface, and this would cause a considerable difference in pressure coefficient $C_p$ in the leeward zone.

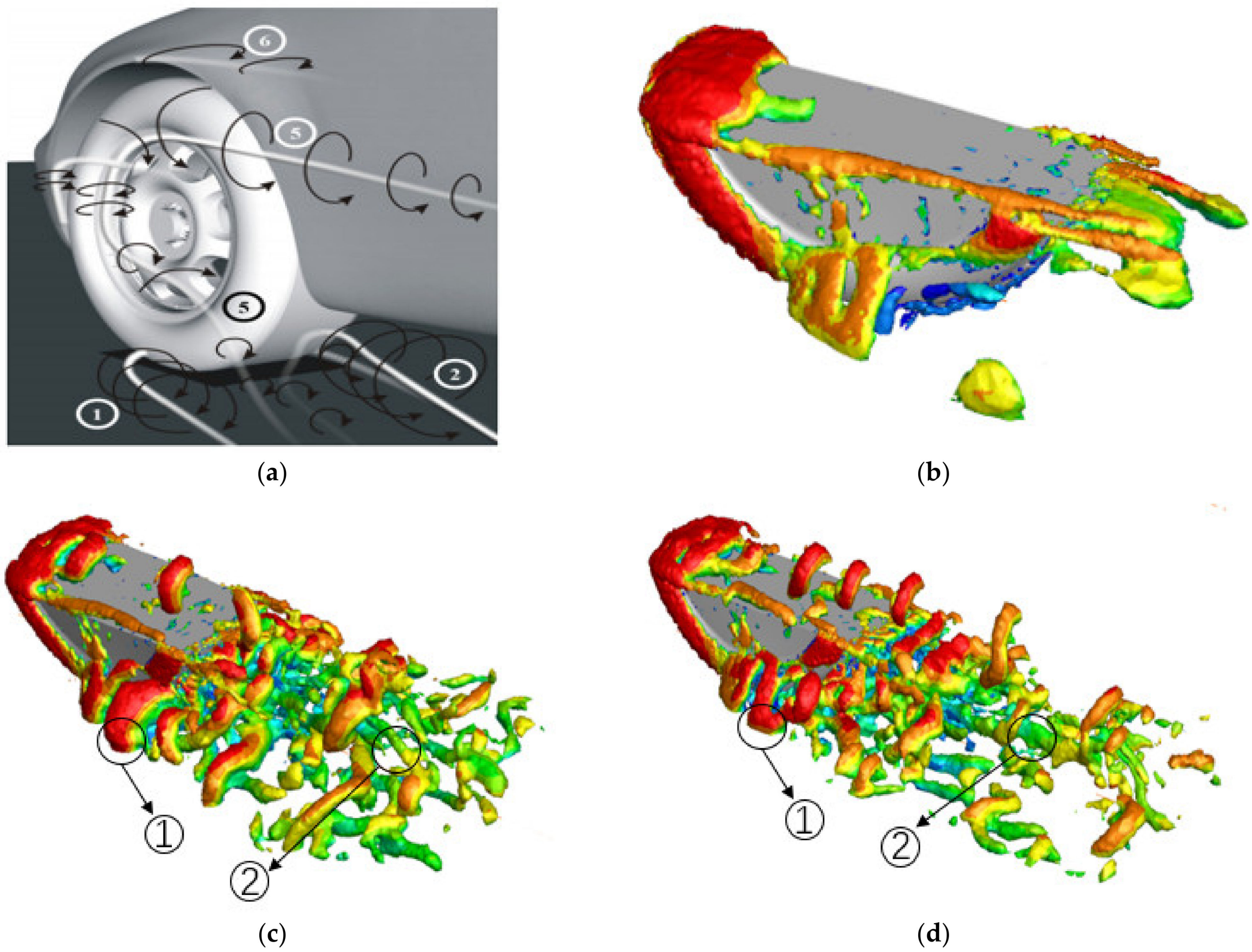


**Figure 19.** Comparisons of instantaneous vortex structures around tire between experiment and simulation. (**a**) Experimental results [22]; (**b**) SST model; (**c**) LES model; (**d**) DES model.

## 6. Conclusions

The surface pressure coefficients and flow field characteristics around a partially statically loaded tire were investigated using SST, LES, and DES turbulence models. Based on the experimental and analytical results, the following conclusions can be drawn:

(1) The surface pressure coefficient $C_p$ of a tire under static load was obtained by conducting the wind tunnel experiment. The $C_p$ values in the longitudinal sections firstly decreased and then increased, then dropped suddenly near the front of the contact patch, and finally attained a relatively steady state with little fluctuation. Besides, along the transverse sections, the $C_p$ values were reduced with upsurges in the distance from the center of the tread.

(2) Compared to the wind tunnel experiment, SST, LES, and DES can predict similar pressure coefficient $C_p$ trends. However, some differences were observed in the leeward zone and the lateral sections. The relative error of the SST model is the maximum at 22.4%, the LES is next, and the DES is the minimum at 14.8%.

(3) The effects of the three turbulence models on the flow around the tire were significant, especially in the leeward zone. Notably, the SST model is not able to capture the instantaneous flow field information, and the LES and DES models can predict the complex wake vortex structures. Considering the differences in surface coefficient $C_p$ obtained using the three turbulence models, the DES model has better predictive ability in capturing the unsteady flow characteristics around a statically loaded tire.

**Author Contributions:** Conceptualization, H.Z. and H.L.; methodology, H.Z.; software, H.Z. and H.L.; validation, H.Z., H.L., and L.Z.; formal analysis, Q.C.; investigation, H.L.; resources, H.Z.; data curation, H.L.; writing—original draft preparation, H.Z.; writing—review and editing, H.Z. and H.L.; visualization, Q.C.; supervision, L.Z.; project administration, H.Z.; funding acquisition, H.Z. All authors have read and agreed to the published version of the manuscript.

**Funding:** This research was funded by the National Natural Science Foundation of China (No.52072156, No. 51605198) and the Postdoctoral Foundation of China (No.2020M682269).

**Institutional Review Board Statement:** Not applicable.

**Informed Consent Statement:** Not applicable.

**Data Availability Statement:** Not applicable.

**Conflicts of Interest:** The authors declare no conflict of interest.

## References

1. Hobeika, T.; Sebben, S. Tyre pattern features and their effects on passenger vehicle drag. *SAE Int. J. Passeng. Cars-Mech. Syst.* **2018**, *11*, 401–413. [CrossRef]
2. Kawamata, H.S.; Kuroda, S.T.; Oshima, M. *Improvement of Practical Electric Consumption by Drag Reducing under cross Wind*; SAE Techical Paper 2016-01-1626; SAE International: Warrendale, PA, USA, 2016.
3. Wickern, G.; Zwicker, K.; Pfadenhauer, M. Rotating wheels-their impact on wind tunnel test techniques and on vehicle drag results. *SAE Trans.* **1997**, *106*, 254–270.
4. Brandt, A.; Berg, H.; Bolzon, M.; Josefsson, L. *The Effects of Wheel Design on the Aerodynamic Drag of Passenger Vehicles*; SAE Techical Paper 2019-01-0662; SAE International: Warrendale, PA, USA, 2019.
5. Fackrell, J.E. The Aerodynamics of an Isolated Wheel Rotating in Contact with the Ground. Ph.D. Thesis, University of London, Landon, UK, 1974.
6. Landström, C.; Walker, T.; Löfdahl, L. *Effects of Ground Simulation on the Aerodynamic Coefficients of a Production Car in Yaw Cond*; Techical Paper 2010-01-0755; SAE International: Warrendale, PA, USA, 2010.
7. Wittemeier, F.; Willey, P.; Kuthada, T.; Widdecke, N.; Wiedemann, J. Classification of aerodynamic tyre characteristics. In Proceedings of the International Vehicle Aerodynamics Conference, Loughborough, UK, 14–15 October 2014.
8. Hobeika, T.; Sebben, S.; Landstrom, C. Investigation of the influence of tyre geometry on the aerodynamics of passenger cars. *SAE Int. J. Passeng. Cars-Mech. Syst.* **2013**, *6*, 316–325. [CrossRef]
9. Breńkacz, Ł.; Bagiński, P.; Żywica, G. Experimental research on foil vibrations in a gas foil bearing carried out using an Ultra-High-Speed Camera. *Appl. Sci.* **2021**, *11*, 878. [CrossRef]
10. Abdulwahab, M.R.; Ali, Y.H.; Habeeb, F.J.; Borhana, A.A.; Abdelrhman, A.M.; Al-Obaidi, S.M.A. A review in particle image velocimetry techniques (developments and applications). *J. Adv. Res. Fluid Mech. Therm. Sci.* **2020**, *65*, 213–229.
11. Axon, L.; Garry, K.; Howell, J. An evaluation of CFD for modelling the flow around stationary and rotating isolated wheels. *SAE Trans.* **1998**, *107*, 205–215.
12. Wang, F.; Yin, Z.; Yan, S.; Zhan, J.; Friz, H.; Li, B.; Xie, W. Validation of Aerodynamic Simulation and Wind Tunnel Test of the New Buick Excelle GT. *SAE Int. J. Passeng. Cars-Mech. Syst.* **2017**, *10*, 195–202. [CrossRef]
13. Link, A.; Widdecke, N.; Wittmeier, F.; Wiedemann, J. Measurement of the aerodynamic ventilation drag of passenger car wheels. *ATZ Worldw.* **2016**, *118*, 38–43. [CrossRef]
14. Patel, C.B.; Goyal, S.; Gupta, B.; Saraswat, A. *Aero-Acoustics Noise Prediction of 3d Treaded Tyre Using Cfd*; SAE Techical Paper 2019-26-0362; SAE International: Warrendale, PA, USA, 2019.
15. Schnepf, B.; Schütz, T.; Indinger, T. Further investigations on the flow around a rotating, isolated wheel with detailed tread pattern. *SAE Int. J. Passeng. Cars-Mech. Syst.* **2015**, *8*, 261–274. [CrossRef]
16. Wei, Z.; Yang, W.; Xiao, R. Pressure fluctuation and flow characteristics in a two-stage double-suction centrifugal pump. *Symmetry* **2019**, *11*, 65. [CrossRef]
17. Diasinos, S.; Doig, G.; Barber, T.J. On the interaction of a racing car front wing and exposed wheel. *Aeronaut. J.* **2014**, *118*, 1385–1407. [CrossRef]
18. McManus, J.; Zhang, X. A computational study of the flow around an isolated wheel in contact with the ground. *J. Fluid Eng.* **2006**, *128*, 520–530. [CrossRef]
19. Huang, M.; Zhou, H.; Li, K.; Wang, G. A calculational aero-acoustic study of spokes of an isolated nonpneumatic tire. *Tire Sci. Tec.* **2020**, *48*, 46–61. [CrossRef]
20. Ramachandran, D.; Doig, G.C. Unsteady Flow around an Exposed Rotating Wheel. Ph.D. Thesis, University of New South Wales, Sydney, Austrailia, 2012.
21. Salati, L. Detached Eddies Simulations on a Fully Exposed Rotating Wheel in Contact with a Moving Ground. Master's Thesis, University of New South Wales, Sydney, Australia, 2012.

22. Dassanayake, P.R.K.; Ramachandran, D.; Salati, L.; Barber, T.J.; Doig, G.C. Unsteady computational simulation of the flow structure of an isolated wheel in contact with the ground. In Proceedings of the 18th Australasian Fluid Mechanics Conference, Launceston, Australia, 3–7 December 2012.
23. Wäschle, A. *The Influence of Rotating Wheels on Vehicle Aerodynamics-Numerical and Experimental Investigations*; SAE Techical Paper 2007-01-0107; SAE International: Warrendale, PA, USA, 2007.
24. Zhou, H.; Wang, G.; Ding, Y.; Yang, J.; Liang, C.; Fu, J. Effect of friction model and tire maneuvering on tire-pavement contact stress. *Adv. Mater. Sci. Eng.* **2015**, *2015*, 1–11. [CrossRef]
25. Zhou, H.; Jiang, Z.; Wang, G.; Zhang, S. Aerodynamic Characteristics of Isolated Loaded Tires with Different Tread Patterns, Experiment and Simulation. *Chin. J. Mech. Eng.* **2021**, *34*, 1–16. [CrossRef]
26. Roul, R.; Kumar, A. Fluid-structure interaction of wind turbine blade using four different materials, numerical investigation. *Symmetry* **2020**, *12*, 1467. [CrossRef]
27. Liu, Q.; Dong, Y.; Lai, H. Large eddy simulation of compressible parallel jet flow and comparison of four subgrid-scale models. *J. Appl. Fluid. Mech.* **2019**, *12*, 1599–1614. [CrossRef]
28. Gritskevich, M.S.; Garbaruk, A.V.; Schütze, J.; Menter, F. Development of DDES and IDDES formulations for the k-$\omega$ shear stress transport model. *Flow Turbul. Combust.* **2012**, *88*, 431–449. [CrossRef]
29. Parfett, A. Flow around Cambered and Yawed Pneumatic Tyres. Ph.D. Thesis, University of Cambridge, Cambridge, UK, 2020.
30. Dubief, Y.; Delcayre, F. On coherent-vortex identification in turbulence. *J. Turbul.* **2000**, *11*, 1–23. [CrossRef]
31. Wu, Y.; Zhang, W.; Wang, Y.; Zou, Z.; Chen, J. Energy dissipation analysis based on velocity gradient tensor decomposition. *Phys. Fluids* **2020**, *32*, 035114.